crystals

MDPI

Article

Gemological and Mineralogical Studies of Greenish Blue Apatite in Madagascar

Zhi-Yi Zhang, Bo Xu *, Peng-Yu Yuan and Zi-Xuan Wang

School of Gemmology, China University of Geosciences Beijing, 29 Xueyuan Road, Haidian District, Beijing 100083, China; 1009191124@cugb.edu.cn (Z.-Y.Z.); yuanpengyu@cugb.edu.cn (P.-Y.Y.); wangzx@cugb.edu.cn (Z.-X.W.)

* Correspondence: bo.xu@cugb.edu.cn

Abstract: Madagascar is known as the 'Island of Gemstones' because it is full of gemstone resources. Apatite from Madagascar is widely popular because of its greenish blue Paraiba-like color. This study analyzes apatite from Madagascar through standard gemological characteristic methods, spectroscopic tests and chemical analyses (i.e., electron probe and laser ablation inductively coupled plasma mass spectrometry). This work explores the gemological and the diagenesis information recorded on Madagascar apatite by comparing them with apatite from other sources and establishes the origin information of Madagascar apatite. The origin characteristics are as follows: Apatite from Madagascar is fluorapatite, with excellent diaphaneity, greenish–blue color caused by Ce and Nd and crystal structure distortion indicated by spectroscopic tests. The F/Cl ratio (16.47 to 21.89) suggests its magmatic origin Cl loss during the weathering processes forming the source rocks, and lg fO_2 (−10.30 to −10.35) reflects the high oxidation degree of magma.

Keywords: gemological; mineralogical; greenish blue apatite; fluorapatite

Citation: Zhang, Z.-Y.; Xu, B.; Yuan, P.-Y.; Wang, Z.-X. Gemological and Mineralogical Studies of Greenish Blue Apatite in Madagascar. *Crystals* **2022**, *12*, 1067. https://doi.org/10.3390/cryst12081067

Academic Editors: Vladislav V. Gurzhiy and Jolanta Prywer

Received: 22 June 2022
Accepted: 23 July 2022
Published: 30 July 2022

1. Introduction

Apatite is a chain phosphate mineral ($CaPO_4$); the high-quality ones are considered semi-precious gemstones [1]. Apatite has no preferential precipitation temperature; hence, it is a common accessory mineral widely distributed in Earth's crust and found in magmatic, sedimentary, metamorphic and hydrothermal systems [2–4]. Mafic magmatic rocks contain up to 20–30% of apatite. Apatite is of indicative significance for magma evolution and diagenesis because it is not affected by metamorphism and hydrothermal alteration [5–7]. It is enriched with trace elements and halogen elements, such as iron, manganese, rare earth elements (REE), fluorine and chlorine. The REE content generally ranges from 5% up to 11.4% [8]. These elements not only record and preserve information about the parent magma and indicate the magma's redox state but also assist in identifying and determining the rock type.

Myanmar, Sri Lanka, India, Madagascar and China are among the main sources of apatite. Madagascar mainly produces blue, green and sky-blue gem-quality apatite [1].

Apatite belongs to the hexagonal crystal system, specifically the symmetrical type 6/m. Its chemical formula is $X_5(ZO_4)_3Y$, where X is an ion represented by Ca^{2+}, which can be isomorphically replaced by Mg^{2+}, Fe^{2+}, Sr^{2+}, Mn^{2+}, Pb^{2+}, Zn^{2+}, Ba^{2+}, Ag^{+} and REE^{3+}. Z = P, As, V, Si, S, C, etc. Y is an additional anion [9]. The most common phase in rocks is fluorapatite ($Ca_5[PO_4]_3F$) [10]. Ca^{2+} occupies two kinds of positions in the apatite lattice represented by Ca1 (coordination 9 with nine oxygen ions) and Ca2 (coordination 7 with six oxygen ions and an additional anion). The number ratio of Ca1 and Ca2 is 4:6, and their ion radii are 1.18 Å and 1.06 Å, respectively [8]. Apatite structure can tolerate relatively large structural distortions and allow different substitutions [11]. Light REE preferably occupy the Ca2 site [12]. Na^{+}, Eu^{2+}, Fe^{2+}, Mg^{2+}, Pb^{2+}, Mn^{2+}, Sr^{2+}, REE^{3+}, U^{4+} and Th^{4+} occupy the X site, Si^{4+}, S^{6+} and C^{4+} tend to occupy the Z site. Na^{+} is usually situated at the Ca1 site.

It can access fluorapatite through three substitutions (below, where V = vacancy) [12–14]: $REE^{3+} + Na^{+} = 2Ca^{2+}$; $Na^{+} + S^{6+} = Ca^{2+} + P^{5+}$; and $2Na^{+} = Ca^{2+} + [V]$. Due to the law of charge conversation, the monovalent ion addition is indicated in the existence of alternative ionic groups, such as REE^{3+} and SO_4^{2-}. REE^{3+} and Y^{3+} can occur in higher concentrations and occupy the Ca2 site. The possible alternative reactions for REE^{3+} and Y^{3+} are as follows [11,12,15–17]: $REE^{3+} + Mn^{2+} + Na^{+} = 3Ca^{2+}$; $REE^{3+} + SiO_4^{4-} = Ca^{2+} + PO_4^{3-}$ and $REE^{3+} + O^{2-} = Ca^{2+} + F^{-}$. Divalent ions can be doped into apatite at any concentration because they have a common charge and a similar cation size as Ca^{2+}. In natural apatite, the most abundant tetravalent ions (i.e., Th^{4+} and U^{4+}) can enter apatite through the following complex substitution [11,18–20]: $Th^{4+}(U^{4+}) + [V] = 2Ca^{2+}$. The PO_4^{3-} ion cluster can be substituted by the AsO_4^{3-}, SO_4^{2-}, CO_3^{2-} and SiO_4^{4-} ion clusters [21–24]. The following substitutions can occur for an instance of SO_4^{2-} [22]: $SO_4^{2-} + SiO_4^{4-} = 2PO_4^{3-}$ and $SO_4^{2-} + Na^{+} = PO_4^{3-} + Ca^{2+}$.

As accessory minerals, apatites could provide an extremely reliable record of magma conditions and preserve in the sedimentary record in order to document the formation and evolution of magmas now lost in the geological record. Elements supporting varying states in accessory minerals can reflect the redox conditions through the valence state. Fe, Mn, Ce and Eu offer great potential in obtaining robust estimates of redox conditions. For instance, Ce in zircon has been studied for its relationship to fO_2, an indicator of the availability and ability of oxygen to participate in mineral and liquid reactions [25].

In this study, gem-quality apatite crystal samples from Madagascar were selected, and gemological and spectroscopy tests were performed to determine specific types. The results obtained herein are useful for subsequent studies on and developments of apatite. Given the gaps in the gemological and spectroscopic studies of Madagascar apatite, in this study, the gemological and spectroscopic analyses will be more detailed, providing a theoretical basis for the forthcoming research of blue to green−blue Paraiba-like apatite and establishing the origin information of Madagascar apatite.

2. Geological Setting

Located in southeastern Africa, Madagascar is the fourth largest island in the world. It is formed by the cleavage of Gondwanaland, part of the African craton, and it is mainly composed of Precambrian tectonic-magmatic-metamorphic heterogeneous rocks, Late Paleozoic–Mesozoic silty clastic carbonate rocks and Mesozoic volcanoes–sedimentary rock systems [26]. Among them, the Precambrian hybrid rocks are widely distributed, accounting for approximately 75% of the total area (Figure 1). Recent studies have shown that the Precambrian here mainly experienced tectonic–thermal events, such as Archaic-Paleoproterozoic substrate formation and cover deposition, Middle–Neoproterozoic Continent of Rhodesia's disintegration, oceanic crust subduction, late Neoproterozoic-Early Paleozoic East-West Gondwana continent convergence, collage, collision orogeny and post−orogenic lithospheric demolition [27]. The origin and composition of the plot are very complex [28].

According to previous research, apatite can be produced as an accessory mineral in granite in the Ambatondrazaka region and as a vein mineral in the same region of magma-type vanadium–titanium magnetite [28,29]. The magmatic rocks in this area are developed in the form of bands and rock plants, spreading in the north-west and -east directions, mainly in the north-west direction. The granite outcrop area is 50 km^2, making it possible for apatite to be exploited. Magma-type V-Ti magnetite is mainly produced in Precambrian super-base hybrid rocks [29]. Further gemological and mineralogical studies on apatite from Madagascar are presented herein (Figure 2).

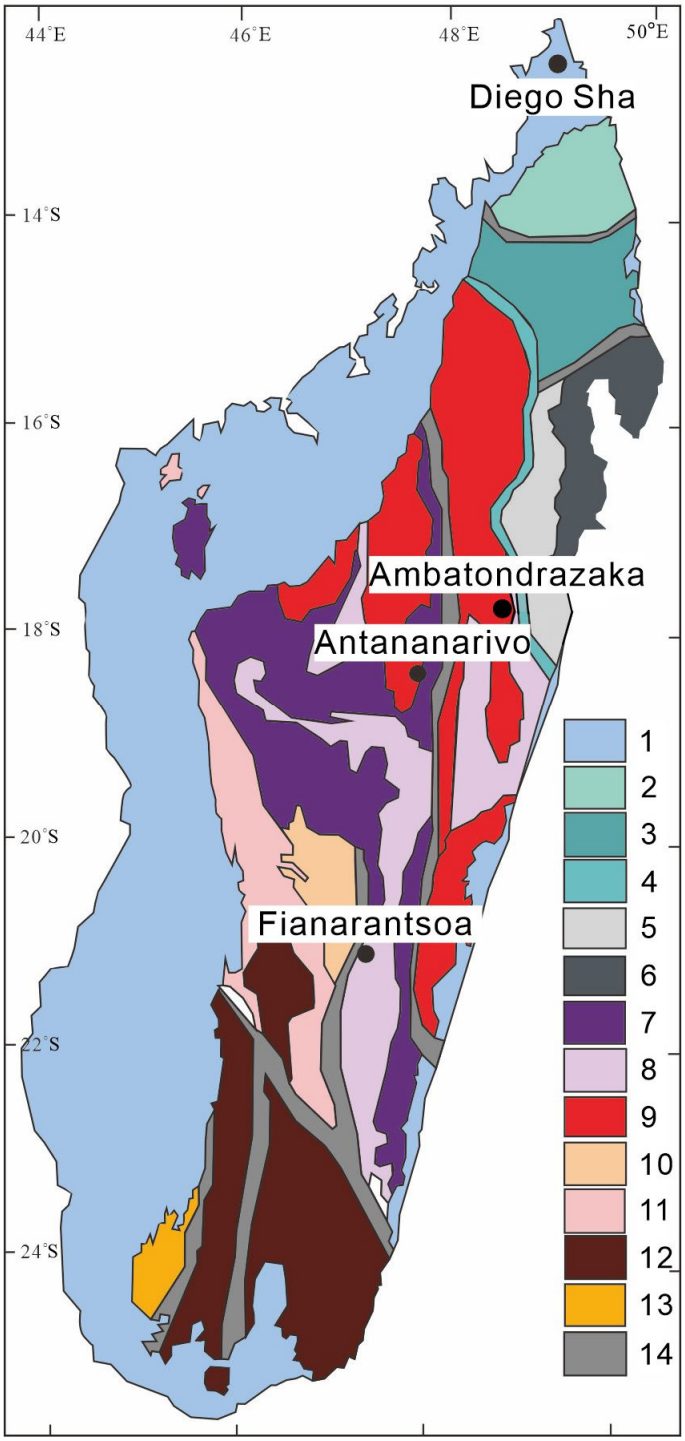

Figure 1. Madagascar map: outline of the structural–lithological units during the Precambrian Period. 1. Sedimentary strata. 2. Daraina Supergroup, Manambata Rock Set. 3. Sahantaha Group, North Antsirabe Rock Formation (Bemarivo units 2 and 3). 4. Betsimisaraka Snake Green Mixed Rock Belt. 5. Ambodiriana Group, Nosy Boraha Rock Formation. 6. Mananara Group, Masoala Rock Sets (Antongil units 5 and 6). 7. Granite mixed gneiss. 8. Graphite metamorphic rocks (Antananarivo units 7 and 8). 9. Tsaratanana Greenstone Belt. 10. Itermo group. 11. Amborompotsy Group (10 and 11 for Itremo units). 12. Vohibory group. 13. Androyen Anosyen blocks (12 and 13 for the Tsivory unit). 14. Cutting tapes: Ant: Antsaba; San: Sandratota; Agv: Angove; Bet: Betsileo; Ran: Ranotsara; Apm: Ampanihy; and Ber: Beraketa. From [26].

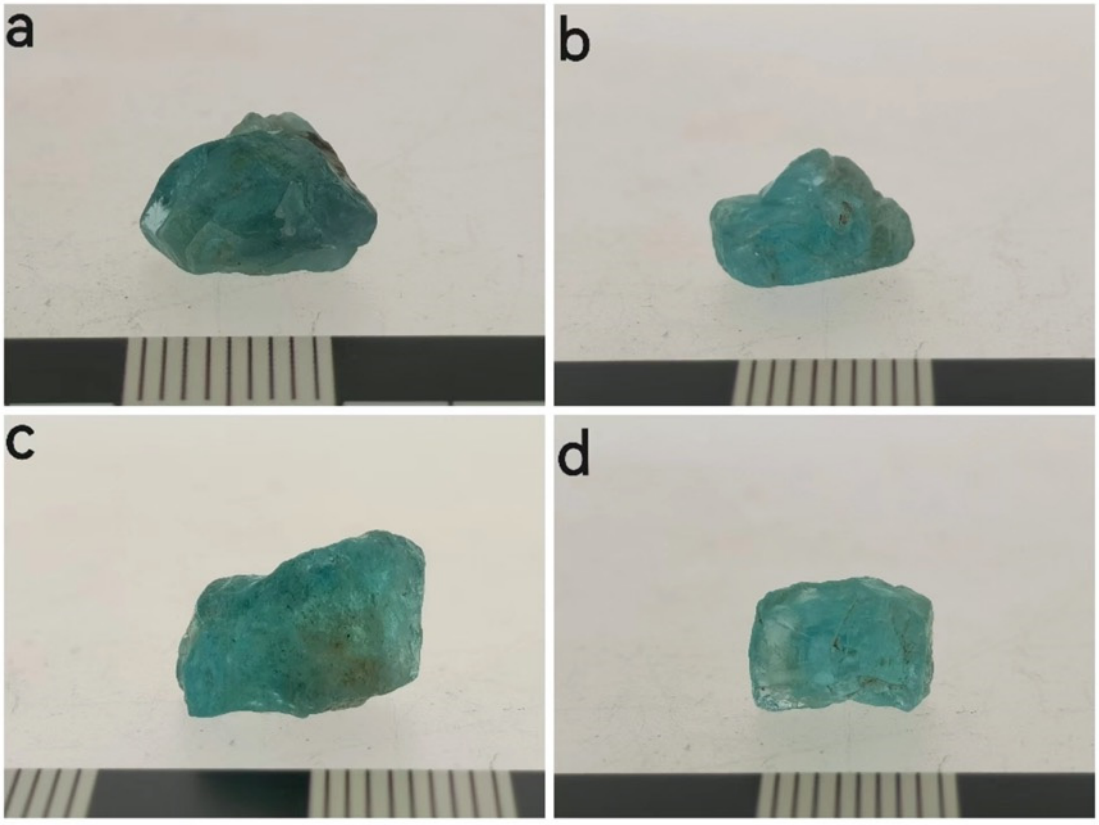

Figure 2. (**a**–**d**) Apatite crystals MADB-1 to MADB-4 from Madagascar. One millimeter per line.

3. Materials and Methods

Four apatite samples (i.e., MADB-1–MADB-4, Figure 2) from Madagascar were subjected to standard gemological tests.

The classic gemological analyses were carried out at the Gemological Research Laboratory of China University of Geosciences, Beijing, including observation, RI, ultraviolet fluorescence detection and specific gravity testing. The optical observations were carried out with a tenfold magnification gem microscope. RI was determined using the spot measurement method. The UV fluorescence detection of samples was performed using UV fluorescent lamps with long and short wavelengths. The specific gravity was tested by the hydrostatic method, and each sample was tested thrice.

The IR analyses were carried out with a Tensor 27 Fourier infrared spectrometer (Bruker, Karlsruhe, Germany) using the reflection method. The test conditions were as follows: 18–25 °C scanning temperature; <70% humidity; 85–265 V scanning voltage; 4 cm^{-1} resolution; 6 mm grating; 400–2000 cm^{-1} test range; and 32 times of scanning signal accumulation.

Raman spectroscopy was performed with the HR Evolution Raman microspectrometer (HORIBA, Kyoto, Japan) with the following analytical conditions: 532 nm laser wavelength; 200–2000 cm^{-1} scanning range; 50 mW laser power; 4 cm^{-1} resolution; 100 μm slit width; 600 gr/mm grating; 4 s scanning time; and 3 s integration time.

A UV-3600 UV-VIS spectrophotometer (Shimadzu Corporation, Kyoto, Japan) with a reflection method was used to perform the UV-VIS spectroscopy tests. The method conditions were as follows: 200–900 nm wavelength; 20 nm slit width; 1.0 s time constant; medium scanning speed; and 0.5 s sampling interval.

A homogeneous portion of the apatite samples without inclusions was selected for testing to obtain a more representative elemental content.

We selected six spots at MADB-1 and -2 and three spots for each sample. The apatite crystals were first mechanically crushed. The pure inner parts of the sample were then

selected under a binocular microscope and placed in an epoxy block to be polished to maximum surface. Before the analyses, the polishing portion was carbon-blasted on the surface. The elements were measured using a JXA-8230 electron probe microanalyser (JEOL, Tokyo, Japan) at Macquarie University, Australia. The following test conditions were applied: 2×10^{-8} A electron beam current; 15.0 kV accelerating voltage; and 5 µm beam spot. Each element was tested with an accuracy greater than 0.001% and corrected by ZAF calibration.

The trace element compositions were measured using laser ablation inductively coupled plasma mass spectrometer in the Institute of Geomechanics, Chinese Academy of Geological Sciences. Inline testing was performed using a 193 nm excimer laser ablation system (GeoLas HD; Coherent, Santa Clara, CA, USA) and a four-stage rod mass spectrometer (Agilent 7900, Agilent, Palo Alto, Santa Clara, CA, USA) with the carrier gases of Ar and He. NIST SRM 610 and 612 were used as the external standard, whilst 43Ca was employed as an internal marker for the trace element content.

4. Results

4.1. Visual Appearance and Gemological Properties of Apatite

Apatite samples analyzed in this work were greenish-blue uniform color with a glassy luster. The samples were plate-like or irregular in shape; the diaphaneity was transparent. The crystals show internal fissures, black short-columnar and orange-red inclusions. Moreover, greasy and shiny shell-like and irregular fractures were found. The crystal size ranged from 9 to 12 mm, with 6–10 mm thickness.

The RI of the samples was 1.63–1.64, and all samples were inert at the UV long and short wavelengths. The specific gravity values varied from 3.172 to 3.195.

4.2. Spectral Characteristics

4.2.1. Infrared Spectrum

The infrared spectrum is used for determining the phase of apatite and the presence of crystal distortion in order to establish origin information. Previous literature on apatites showed that infrared spectrum vibration was mainly manifested in the $[PO_4]^{3-}$ ion vibration. Free $[PO_4]^{3-}$ ions had four fundamental frequencies, namely symmetrical telescopic vibration (v_1), bending vibration (v_2), anti−telescopic vibration (v_3) and bending vibration (v_4) [11,13]. The v_2 band came from two strong absorption peaks at 320 and 270 cm^{-1} [9]. The test wavelength was between 2000 and 400 cm^{-1}. The v_2 bend was invisible and is not discussed below.

The following characteristic peaks were found (Figure 3): a weak, single absorption band at 962 cm^{-1} assigned to the symmetric stretching vibration (v_1); a wide, strong absorption shoulder near 1057 cm^{-1}; a strong absorption band at 1101 cm^{-1} assigned to the anti-symmetric stretching vibration (v_3) of $[PO_4]^{3-}$. The moderately strong absorption bands at 575 and 608 cm^{-1} were assigned to the bending vibration (v_4) of the $[PO_4]^{3-}$ ion; a slightly weak absorption band at 591 cm^{-1} was observed in MADB−3 and MADB−4 spectra. This absorption band was also assigned to the bending vibration (v_4) of $[PO_4]^{3-}$.

The R050274 fluorapatite from the RRUFF database was selected for comparison with the Madagascar samples. This sample from Minas Gerais, Brazil, was blue, with two moderately strong v_4 bands at 567 and 600 cm^{-1}, a sharp v_1 band found at 962 cm^{-1} and two v_3 bands near 1022 cm^{-1} and 1090 cm^{-1}. Comparing the MADB samples with R050274, we found an extra 591 cm^{-1} weak analyzed band because of the orientation. It was also assigned to v_4 vibration of $[PO_4]^{3-}$. The v_3 vibration of $[PO_4]^{3-}$ showed an obvious right shift, and the v_3 bands widened. The splitting of the P−O bond and the interaction of the $[PO_4]^{3-}$ tetrahedron vibration pattern with the crystal lattice of fluorapatite have been responsible for the v_3 band widening [30]. In addition, the infrared spectra results of the MADB samples were consistent with fluorapatite. Therefore, apatite of Malagasy origin could preliminarily be judged as fluorapatite, and there is splitting of P−O bond in fluorapatite crystal lattice indicated by infrared spectrum.

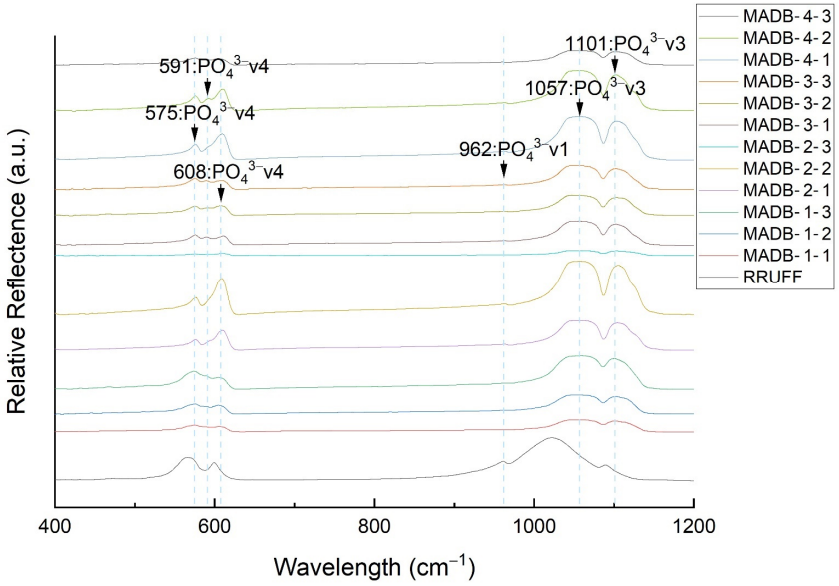

Figure 3. Infrared spectra of the Madagascar apatite samples.

4.2.2. Raman Spectra

The Raman spectra of the Madagascar apatite appeared at 400−1500 cm^{-1} [8]. The Raman feature bands of the samples were chiefly reflected in the vibration of the $[PO_4]^{3-}$ ion cluster [31]. The symmetric stretching vibration (v_1) bands of the ion cluster were seen at 962–965 cm^{-1}. The bending vibration (v_2) bands were observed at 419–431 cm^{-1}. Asymmetric stretching vibration (v_3) bands were detected at 1040–1049 cm^{-1}, whilst asymmetric bending vibration(v_4) bands were detected at 575–593 cm^{-1}.

Figure 4 shows the Raman characteristic absorption peaks of the apatite samples. The strongest band at 962 cm^{-1} was assigned to the symmetrical telescopic vibration(v_1) band of $[PO_4]^{3-}$. The symmetrical bending vibration band (v_2) at 430 cm^{-1} was a weak band. Bands were found near 1052 cm^{-1} and 1086 cm^{-1}, which were assigned to the asymmetric stretching vibration of $[PO_4]^{3-}$. In addition, a medium-strong absorption band at 591 cm^{-1} assigned to the asymmetric bending vibration (v_4) was also observed. Since its Raman spectrum matches the standard Raman spectrum of fluorapatite well, the crystals from Madagascar resulted in fluorapatites, which confirms the results of infrared spectra.

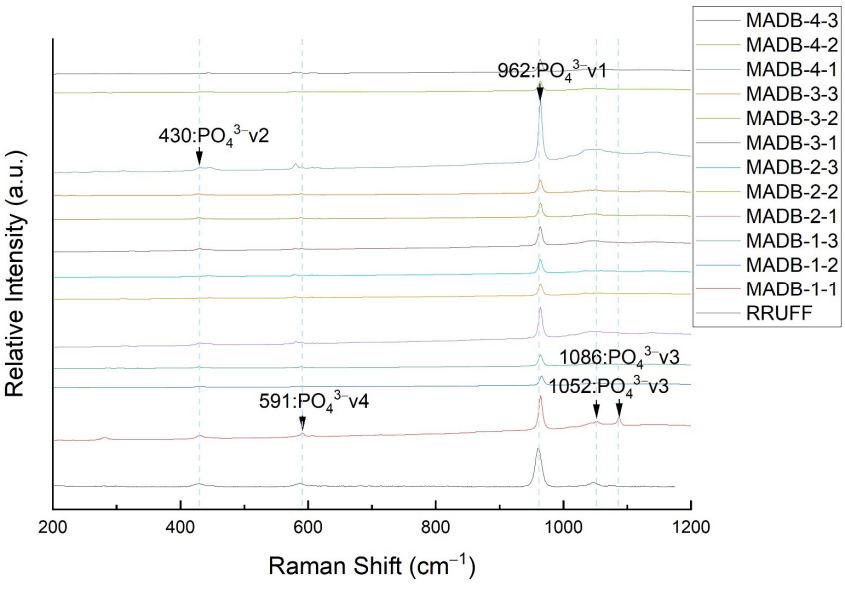

Figure 4. Raman spectra of the Madagascar apatite samples.

4.2.3. UV-VIS Spectrum

The types and contents of REE directly affect the gemological properties of apatite, such as color and luminescence. We can determine the causes of the different colors of apatite through the UV-VIS spectrum and indirectly determine REE content in Madagascar apatite. Apatite with a high REE content absorbs more strongly in the ultraviolet region. This is mainly related to the high content of light REE (LREE) ions [8]. As the concentration of REE, the apatite absorption of visible increases. Figure 5 shows the MADB apatite UV-VIS spectra.

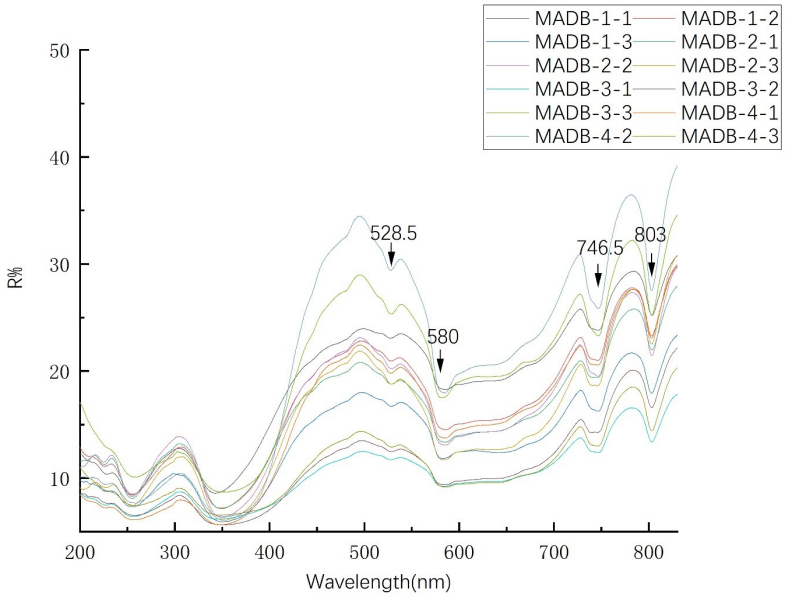

Figure 5. UV-VIS spectra of the Madagascar apatite samples.

The UV-VIS spectrum revealed that the samples have significant absorptions between 580 nm and 700 nm. Strong reflections were found in 400–550 nm and 700–850 nm, that is, the green, blue−violet and near-infrared regions. The reflectivity in the ultraviolet region was generally low due to the strong absorption of Ce in the ultraviolet region. Moreover, compared with other rare earth elements, Ce has a more significant effect on the weakening of absorption in the blue and orange-red regions [8]. The visible region had moderately pronounced reflectance troughs near 580 nm and 528.5 nm, whilst the infrared region showed sharp, strong hollow near 746.5 nm and 803 nm related to the Nd^{3+} ion absorption [13]. In a word, the color mechanism of MADB apatite was selective absorption of Ce and Nd in the orange-red areas and the ultraviolet regions. The appearance color and the UV-VIS spectrum can corroborate each other. Additionally, the absorptions at 528.5 nm, 580 nm, 746.5 nm and 803 nm can be one of the origin characteristics of Madagascar apatite.

4.3. Major and Trace Elements

Tables A1 and A2 present the major and trace elements of the analyzed apatite crystals. On the basis of the analytical results, the main chemical components of Madagascar apatite were CaO (54.16–54.92 wt%) and P_2O_5 (39.10–40.79 wt.%). The results were consistent with the compositional range of pyrogenic apatite (CaO = 54–57 wt.% and P_2O_5 = 39–44 wt.%) described by Belousova [4].

According to the EPMA results, the chemical formula of MADB−1 was calculated to be $(Ca_{4.499}, Na_{0.015}, Mn_{0.002}, Sr_{0.013}, Ce_{0.012})[P_{2.605}Si_{0.047}S_{0.009}O_{12}](F_{0.804}, Cl_{0.022})$, whilst that of MADB−2 was $(Ca_{4.513}, Na_{0.006}, Sr_{0.009}, Ce_{0.012})[P_{2.607}Si_{0.052}S_{0.010}O_{12}](F_{0.780}, Cl_{0.025})$, which is that of fluorapatite.

The trace elements in the Madagascar apatite included REE, Mn, Sr, Fe and Th. The samples contained 250–270 ppm of Mn, 2900–3095 ppm of Sr, 350–370 ppm of Fe and

665–900 ppm of Th. The total REE content of samples was 9000–10225 ppm. The LREE content was 8690–9860 ppm. The analytical results showed that in the chondrite standardization model (Figure 6), the LREE were slightly enriched, and the HREE were relatively deficient. The δEu range was 0.62–0.66, showing a weak negative Eu anomaly. δCe ranged from 0.94 to 1.00 with no obvious Ce anomaly [32].

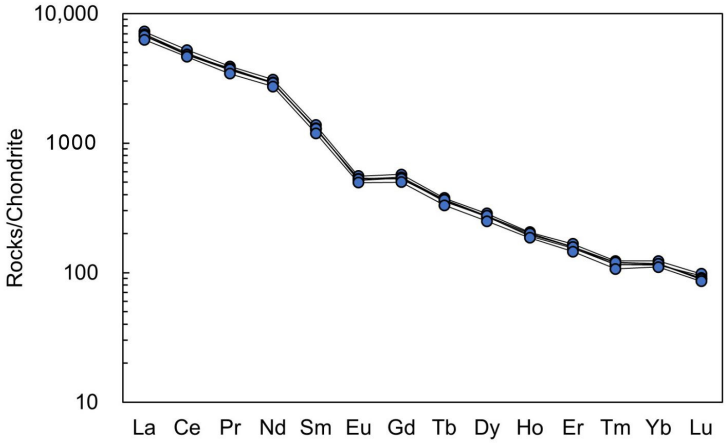

Figure 6. Chondrite-normalized REE distribution patterns of Madagascar apatite. The normalization values for chondrite were from Herman (1971) [33].

5. Discussion

5.1. Gemological Characteristics

In this part, apatites from Madagascar, Morocco, Mexico and China (Shanxi, Shaanxi, Anhui) were in comparison (Table A3). The color of the Madagascar apatite analyzed in this study was greenish blue, which is considered optimal in apatite gem evaluations. Apatites from other origins are yellow or green. Madagascar apatite diaphaneity is better than any other origin's in comparison. The SG of Madagascar apatite was slightly lower than that of the apatite from other origins. Apatites from Madagascar and China (Shanxi and Shaanxi) were inert at the UV, while those from Mexico, Morocco and China (Anhui) had varying degrees of fluorescence. The shape of Madagascar apatite was plate-like or anhedral instead of hexagonal columnar from Shanxi, China.

5.2. Major and Trace Elements

5.2.1. Major Elements Characteristics of Apatite

The previous studies [31,34–36] tested the following apatite samples: Durango in an iron mine from Mexico; Moro in igneous phosphate block rock from Morocco; SDG in an alkaline mafic complex, XZ in mafic sill and M1 in phosphorite-type rare earth deposit from China; ASP-I in Quaternary ignimbrites from Japan. The relationship between SiO_2, FeO and MnO contents in apatite can reflect the apatite origin [31,37,38]; therefore, the MADB apatite were plotted against those from the other sources (Figure 7). The plots confirm the magmatic origin of the blue–green apatite analyzed in this work.

The F content of apatite in Madagascar ranged from 3.10 wt.% to 3.90 wt.%, and the Cl content ranged from 0.17 wt.% to 0.19 wt.% (Appendix A Table A1), showing that the MADB apatite is fluorapatite. The Madagascar apatite had a high F/Cl ratio (16.47 to 21.89) compared with apatite from Mexico, Morocco and Japan (Figure 8, Table A4). The Cl content in the apatite was directly related to the Cl content in the parent magma, suggesting that the Madagascar magma had a lower Cl content than magma from the other regions. F was difficult to remove due to its low solubility in water. Therefore, the rock mass remelted in the crust often exhibited F-rich and Cl-poor characteristics reflected in the F and Cl compositions of apatite [39]. The MADB apatite was verified to be of magmatic origin [40,41]. Sha et al. (2018) verified that the high F/Cl ratio is also related to the Cl loss during the weathering processes forming the source rocks [13].

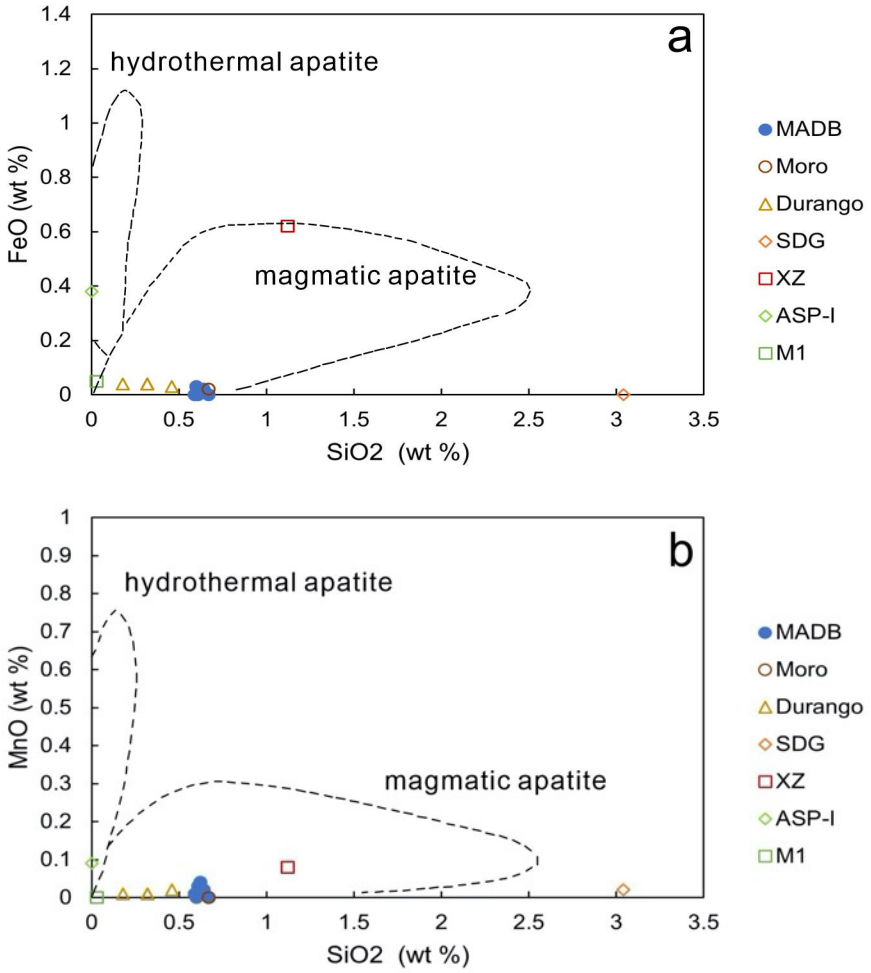

Figure 7. Illustration of the origin of the Madagascar apatite and those from other sources [31,34]: (**a**) FeO–SiO_2 and (**b**) MnO–SiO_2.

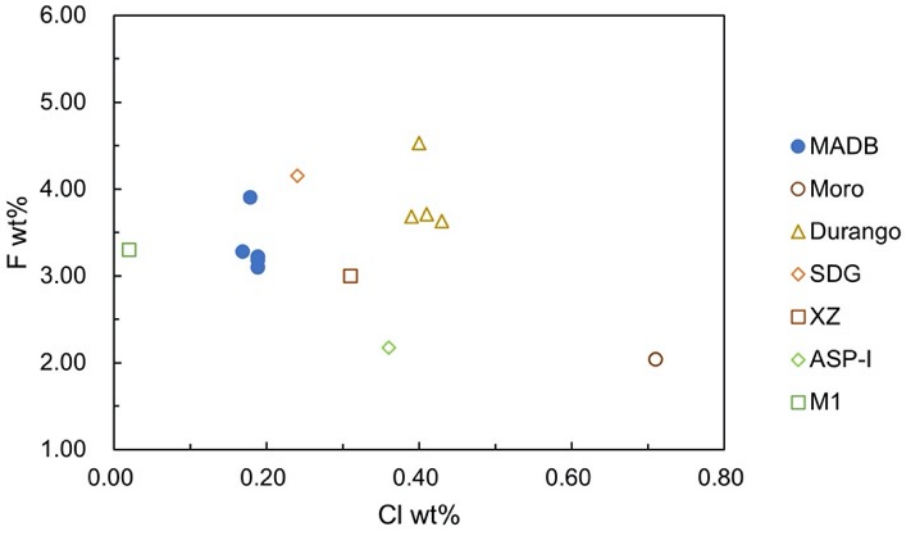

Figure 8. F versus Cl wt% in apatite from different origins.

5.2.2. Rare Earth Element Characteristics of Apatite

The trace element data for apatite showed that apatite can accommodate a wide range of structural distortion due to chemical substitutions [25] (Tables A2 and A5).

The chondrite-normalized REE distribution patterns of apatite usually show negative slopes (high $(Ce/Yb)_N$), indicating a relative enrichment in the LREE (Figure 9) [4]. The Madagascar apatite had $(Ce/Yb)_N$ equaling 41.07–43.36, showing its LREE enrichment (Figure 10). The Moro and Durango samples had $(Ce/Yb)_N$ equaling 24.51 and 18.52–27.21, respectively. M1 apatite only had that equaling 2.68. In general, the δCe of igneous apatite was almost equal to 1, indicating the absence of an obvious Ce anomaly. However, microcrystalline apatite M1 from sedimentary carbonate rocks showed a negative Ce anomaly, which could be one of the differences between the igneous and sedimentary apatite. In contrast, a negative Eu anomaly was found in the magmatic apatite samples (i.e., Durango, Moro and MADB), whilst the M1 apatite had a weak negative Eu anomaly, and the SDG apatite had no obvious Eu anomaly. Conversely, the ΣREE in magmatic apatite were much more abundant compared to the sedimentary apatite. As shown in the slope in Figure 9, the distribution of the REE content of the sedimentary apatite is more uniform.

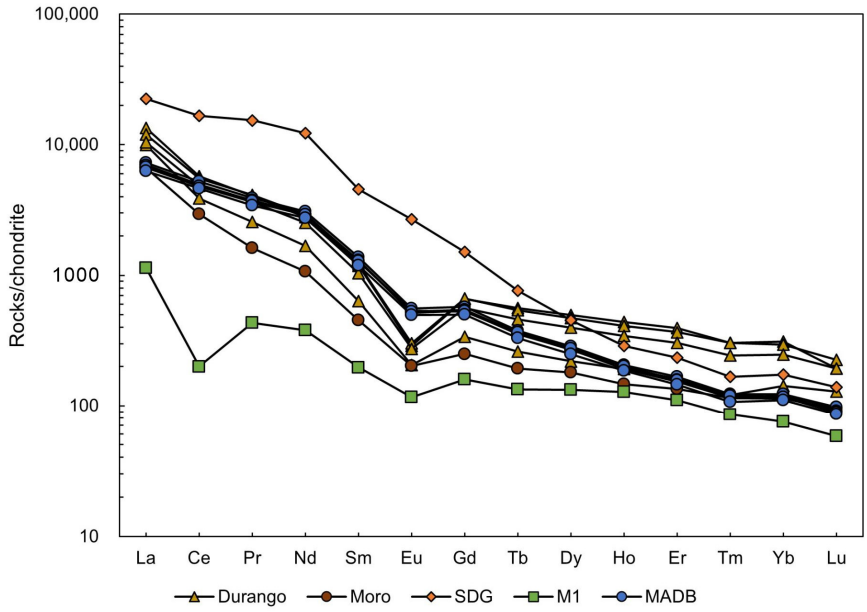

Figure 9. Chondrite-normalized REE distribution patterns of the apatite from Madagascar analyzed in this work compared to apatite from literature. Data from [31,34,42]. Normalization values for chondrite are from Herman (1971) [33].

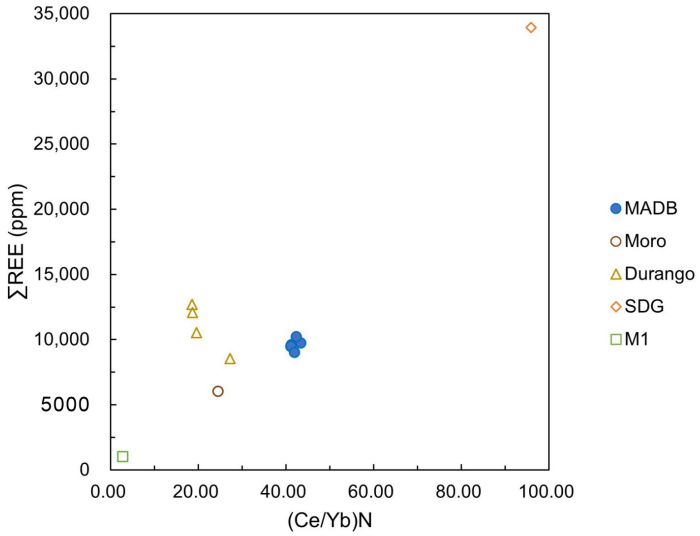

Figure 10. ΣREE versus $(Ce/Yb)_N$ of apatite from different origins.

5.2.3. Redox Characteristics of Magma

The Mn content in the apatite was negatively correlated with the magma oxygen fugacity. Miles et al. [25] proposed an empirical formula for calculating the magma oxygen fugacity with the Mn content in apatite: lg $fO_2 = -0.0022(\pm 0.0003)$ Mn (ppm) $- 9.75(\pm 0.46)$. Introducing the experimental data from the MADB apatite into the formula, we obtained the results of −10.30 to −10.35. Overall, the magma in the Madagascar area had a high oxygen fugacity. Sha et al. [13] also pointed out that apatite with <900 ppm Mn and <2100 ppm Fe had a high oxygen fugacity, which was consistent with the above-mentioned description.

The study of Prowatke et al. [43] indicated that the Mg and Fe contents of apatite were positively related to those of the source magma. The Mg and Fe contents of Madagascar apatite were extremely low, with 21.65–23.44 ppm of Mg and 349.36–372.50 ppm of Fe. It can be rolled out that the magma had very few Mg and Fe elements, which is an iconic feature of felsic magmatic rocks. The XZ and ASP−I apatite were rich in Mg and Fe, corresponding to the characteristics of the parent rock (i.e., XZ was from mafic rocks) [44].

6. Conclusions

After the analyses above, the origin information of Madagascar apatite has been established.

Madagascar apatite crystals have a rare greenish–blue color and excellent diaphaneity, with a low degree of self-formation and slightly lower SG (3.172–3.195). The color mechanism of Madagascar apatite is selective absorption of Ce and Nd in the orange−red areas and the ultraviolet regions indicated by UV–VIS spectrum. In the crystal lattice, there exists splitting of the P–O bond indicated by the infrared spectrum.

According to the spectroscopic and major element analyses, Madagascar apatite is determined as igneous fluorapatite, with an extremely high F/Cl ratio (16.47–21.89). Due to the Cl loss during the weathering processes forming the source rocks, the F/Cl ratio of Madagascar apatite was the highest among the igneous apatite from different origins in comparison, and it also indicates the F-rich and Cl-poor characteristics in the parent rock. In addition, the FeO, MgO and SiO_2 content of Madagascar apatite can also reflect its magmatic origin.

Madagascar apatite has a relatively high LREE enrichment compared with other origins apatite, except SDG. The high $(Ce/Yb)_N$ (41.07–43.36) makes Madagascar apatite different from others. Additionally, the Mn, Mg and Fe concentrations of Madagascar apatite indicated the high oxygen fugacity and the felsic magmatic parent rocks (such as granite in the Ambatondrazaka region).

In summary, the igneous greenish blue apatite from Madagascar has a good scientific value and can be further studied as a standard sample.

Author Contributions: Writing—original draft, Z.-Y.Z.; writing—review and editing, Z.-Y.Z., B.X., P.-Y.Y. and Z.-X.W.; investigation, B.X.; data curation, Z.-Y.Z.; software, Z.-Y.Z.; methodology, B.X.; resources, B.X. All authors have read and agreed to the published version of the manuscript.

Funding: This research was funded by the National Key Technologies R&D Program 2019YFC0605201, 2019YFA0708602, 2020YFA0714802, National Natural Science Foundation of China (42073038, 41803045), Young Talent Support Project of CAST (IGCP-662), Fundamental Research Funds for the Central Universities (265QZ2021012) and Innovation and Entrepreneurship Training Program for College Students of China University of Geosciences (Beijing) (202211415060).

Data Availability Statement: The data presented in this study are available within the article.

Acknowledgments: This is the 9th contribution of BX to the National Mineral Rock and Fossil Specimens Resource Center. Thanks to the two reviewers and the editors for their comprehensive and professional suggestions.

Conflicts of Interest: The authors declare no conflict of interest.

Appendix A

Table A1. Chemical composition and structural formula of Madagascar apatite, determined by EMPA (in wt%).

	F	Na_2O	CaO	P_2O_5	SO_3	SiO_2	FeO	MnO	Cl	SrO	Ce_2O_3	Total
MADB−1−1	3.28	0.10	54.16	39.68	0.45	0.61	0.00	0.03	0.17	0.21	0.42	99.10
MADB−1−2	3.90	0.11	54.68	39.10	0.41	0.62	0.01	0.04	0.18	0.13	0.42	99.59
MADB−1−3	3.10	0.08	54.92	39.56	0.50	0.64	0.02	0.02	0.19	0.25	0.30	99.57
MADB−2−1	3.18	0.04	54.31	39.71	0.50	0.67	0.00	0.00	0.19	0.15	0.42	99.14
MADB−2−2	3.22	0.06	54.54	40.10	0.50	0.60	0.03	0.00	0.19	0.24	0.38	99.86
MADB−2−3	3.22	0.12	54.26	40.79	0.50	0.59	0.00	0.01	0.19	0.21	0.34	100.22
	Si^{4+}	Fe^{2+}	Mn^{2+}	Ca^{2+}	Na^{+}	F^{-}	Cl^{-}	S^{6+}	Sr^{2+}	P^{5+}	Ce^{2+}	
MADB−1−1	0.047	0.000	0.002	4.503	0.015	0.805	0.022	0.009	0.004	2.607	0.012	
MADB−1−2	0.048	0.001	0.003	4.508	0.016	0.949	0.023	0.008	0.003	2.547	0.012	
MADB−1−3	0.050	0.001	0.001	4.564	0.012	0.760	0.025	0.010	0.005	2.598	0.009	
MADB−2−1	0.047	0.000	0.002	4.503	0.015	0.805	0.022	0.009	0.004	2.607	0.012	
MADB−2−2	0.045	0.000	0.000	4.515	0.006	0.780	0.025	0.010	0.003	2.609	0.012	
MADB−2−3	0.047	0.000	0.001	4.446	0.018	0.779	0.025	0.010	0.004	2.641	0.010	

Table A2. Chemical composition and structural formula of Madagascar apatite, analyzed by LA−ICP−MS.

Element		MADB−1−1	MADB−1−2	MADB−1−3	MADB−1−4	MADB−1−5	MADB−2−1
Mg	ppm	22.50	22.26	22.31	23.44	22.00	21.65
Si	ppm	1.13	0.00	1.13	0.98	0.00	0.00
P	%	28.762672	29.974847	28.265906	28.425884	27.471936	27.462787
Cl	ppm	1530.50	1830.53	1450.26	1229.59	1162.63	962.15
Ca	%	57.194298	57.452847	55.776887	54.186530	54.832854	52.793121
Ti	ppm	0.02	0.04	0.10	0.00	0.33	0.44
Mn	ppm	270.14	271.57	265.52	266.64	252.03	254.65

Table A2. *Cont.*

Element		MADB−1−1	MADB−1−2	MADB−1−3	MADB−1−4	MADB−1−5	MADB−2−1
Fe	ppm	369.65	372.50	350.25	353.04	349.36	353.09
Rb	ppm	0.00	0.00	0.09	0.00	0.00	0.00
Sr	ppm	3093.09	3132.23	3044.83	2944.21	2902.41	2941.15
Zr	ppm	0.00	0.00	0.00	0.00	0.00	0.00
Nb	ppm	0.74	0.92	1.12	1.29	0.69	1.19
Ba	ppm	0.29	0.81	0.80	0.52	0.17	0.52
La	ppm	2231.74	2319.83	2216.59	2145.67	2161.80	2008.82
Ce	ppm	4651.92	4903.57	4529.55	4498.58	4509.20	4353.56
Pr	ppm	447.20	467.68	452.40	437.65	445.81	411.92
Nd	ppm	1769.42	1852.47	1755.73	1735.78	1745.71	1641.37
Sm	ppm	254.67	275.52	258.72	260.48	257.39	237.86
Eu	ppm	39.20	40.59	38.63	37.56	38.42	36.17
Gd	ppm	163.59	177.31	168.50	165.87	164.65	154.73
Tb	ppm	17.93	18.82	18.23	17.75	18.29	16.53
Dy	ppm	83.52	88.63	84.73	84.05	85.11	77.26
Ho	ppm	14.29	14.98	14.68	13.98	14.63	13.55
Er	ppm	33.09	35.00	33.17	32.34	32.93	30.49
Tm	ppm	3.79	4.06	3.96	3.81	3.94	3.52
Yb	ppm	21.68	23.40	22.21	22.14	22.19	20.98
Lu	ppm	2.92	3.04	2.82	2.78	2.75	2.65
Hf	ppm	0.04	0.02	0.03	0.03	0.03	0.03
Ta	ppm	0.01	0.02	0.01	0.02	0.02	0.02
Hg	ppm	0.00	0.00	0.00	0.00	0.00	0.00
Pb	ppm	14.53	18.24	17.54	17.56	17.64	16.70

Table A2. *Cont.*

Element		MADB−1−1	MADB−1−2	MADB−1−3	MADB−1−4	MADB−1−5	MADB−2−1
Th	ppm	665.42	835.65	825.05	819.24	854.73	800.74
U	ppm	22.98	25.80	23.07	22.63	22.93	21.45
ΣLREE	ppm	9394.14	9859.66	9251.60	9115.72	9158.34	8689.70
ΣHREE	ppm	340.80	365.24	348.29	342.71	344.48	319.71
ΣREE	ppm	9734.94	10224.90	9599.89	9458.43	9502.81	9009.41
δEu		0.66	0.63	0.63	0.62	0.64	0.64
δCe		0.97	0.98	0.94	0.97	0.96	1.00

Table A3. Characteristics of apatite from different production areas. Data derived from [31,38].

Origin	Color	Lustre	Diaphaneity	RI	DR	SG	UV	Size	Feature
Madagascar	Greenish blue	Glassy luster	Transparent	1.63−1.64		3.17−3.20	Inert	The largest of which measured 12∗10∗9 mm	Plate-like or anhedral, with internal fissures, flat surface black short−columnar and orange−red inclusions
Durango, Mexico	Uniform yellow−green	Glassy luster	Transparent	1.631−1.636	0.005	3.21	Inert to long−wave; weak yellow to short−wave	The largest of which measured 14.97∗9.47∗7.97 mm	Emerald- and cushion-cut. The cushion-cut stone revealed straight growth zoning. The emerald-cut contained a small liquid feather
Anemzi, Morocco	Yellow−green	Glassy to weak glassy luster	Translucent	1.635−1.640		3.18−3.20	Inert to long−wave; weak purple to short−wave	The largest of which measured 14∗8∗7.97 mm	Hexagonal columnar crystal shape, with many fissures, shell-like or irregular fractures, visible crystal face longitudinal pattern
Shanxi, China	Yellow, dark green to dark blue−green	Glassy luster	Translucent	1.632−1.639	0.004	3.19−3.23	Inert	The largest of which measured 30∗10∗5 mm	Hexagonal columnar or subhexagonal columnar crystal form; high degree of self-formation showing massive or columnar

Table A3. *Cont.*

Origin	Color	Lustre	Diaphaneity	RI	DR	SG	UV	Size	Feature
Shaanxi, China	Gray−green	Glassy luster	Sub−transparent	1.633−1.637	0.004	3.21−3.23	Inert	The largest of which measured 6.5∗4∗4 mm	Massive, with hexagonal columnar crystal form, high degree of self−formation, smooth surface, and poor cleavage
Anhui, China	Light yellow	Glassy luster to weak glassy luster	Transparent to translucent	1.633−1.637	0.004	3.18−3.20	Medium yellow−green	The largest of which measured 15∗4∗5 mm	Sheet-like and plate-like, poorly self-formation, no obvious crystalline shape, longitudinal lines between crystal faces

Table A4. Chemical composition and structural formula of apatite from other origins, determined by EMPA (in wt%). Data derived from [31,34–36,42].

	DurangoChew	DurangoFishier	DurangoGriffin	DurangoHou	Moro	SDG	XZ	ASP−I	M1
F	3.71	3.63	4.53	3.68	2.04	4.15	3.00	2.17	3.30
CaO	53.90	53.99	53.85	53.85	54.10	51.58	54.58	53.89	55.57
P_2O_5	41.88	42.16	41.91	41.91	39.63	34.48	41.57	43.56	38.17
SiO_2	0.46	0.18	0.32	0.32	0.67	3.04	1.12	–	0.03
FeO	0.03	0.04	0.04	0.04	0.02	–	0.62	0.38	0.05
MnO	0.02	0.01	0.01	0.01	0.00	0.02	0.08	0.09	0.00
Cl	0.41	0.43	0.40	0.39	0.71	0.24	0.31	0.36	0.02
SrO	0.05	0.04	0.05	0.05	0.03	1.44	–	–	
MgO	0.04	0.02	0.02	0.02	–	0.01	0.20	0.20	0.06
Ce_2O_3	–	–	–	–	–	–	–	0.28	
Y_2O_3	–	–	–	–	–	–	–	0.32	
Al_2O_3	–	–	–	–	–	–	0.17	–	0.01
ions									
Ca^{2+}	4.667	4.651	4.665	4.648	4.736	4.946	4.389	4.371	4.731

Table A4. *Cont.*

	DurangoChew	DurangoFishier	DurangoGriffin	DurangoHou	Moro	SDG	XZ	ASP−I	M1
Fe^{2+}	0.002	0.003	0.003	0.002	0.001	0.001	0.039	0.024	0.024
Mn^{2+}	0.001	0.001	0.001	0.001	0.000	0.001	0.005	0.006	0.006
P^{5+}	2.865	2.870	2.869	2.877	2.741	2.812	2.641	2.792	2.792
Mg^{2+}	0.005	0.002	0.002	0.004	–	0.000	0.022	0.023	0.007
F^{-}	0.105	0.109	0.102	0.099	0.184	0.014	0.712	0.520	0.520
Cl^{-}	0.056	0.059	0.055	0.053	0.099	0.007	0.039	0.046	0.046

Table A5. Chemical composition and structural formula of Moroccan apatite, analyzed by LA−ICP−MS. Data derived from [31,34,42].

		DurangoChew	DurangoFishier	DurangoGriffin	DurangoHou	Moro	SDG	M1
Rb	ppm	0.12	0.11	0.13	0.12	0.12	0.2	–
Sr	ppm	482	456	491	476	618.13	11368	–
Ba	ppm	1.7	1.4	1.8	1.5	1.29	1.3	–
Nb	ppm	1	0.02	0.03	0.02	0.01	2.4	–
Ta	ppm	0	0	0	0	0	0.03	–
Zr	ppm	1.4	0.6	1.1	0.8	0	48	–
Hf	ppm	0.23	0.19	0.23	0.26	0.01	0.39	–
Pb	ppm	0.9	0.4	0.7	0.6	1.62	50	–
Th	ppm	320	151	270	231	184.37	705	–
U	ppm	20	7	11	11	16.48	47	–
La	ppm	4285	3194	3819	3334	2117.01	7209	364
Ce	ppm	5405	3635	5178	4561	2763.91	15668	188
Pr	ppm	488	307	496	436	193.71	1843	52
Nd	ppm	1677	1009	1745	1514	639.77	7344	227
Sm	ppm	237	127	244	207	90.72	911	39.4
Eu	ppm	21	15	22	20	14.78	196	8.5

Table A5. *Cont.*

		DurangoChew	DurangoFishier	DurangoGriffin	DurangoHou	Moro	SDG	M1
Gd	ppm	204	105	206	174	77.45	468	49.4
Tb	ppm	28	13	27	23	9.68	38	6.7
Dy	ppm	154	68	146	123	55.94	140	41
Ho	ppm	32	14	30	25	10.67	21	9.3
Er	ppm	83	34	77	64	28.34	49	23.2
Tm	ppm	10	4	10	8	3.78	5.5	2.8
Yb	ppm	59	27	56	47	22.79	33	14.2
Lu	ppm	6	4	7	6	2.99	4.3	1.8
Y	ppm	911	427	886	762	–	605	472
ΣLREE	ppm	12113	8269	11504	10072	5819.89	33171	878.9
ΣHREE	ppm	576	269	559	470	211.65	758.8	148.4
ΣREE	ppm	12689	8538	12063	10542	6031.54	33929.8	1027.3
δEu		0.29	0.4	0.3	0.32	0.54	0.92	0.91
δCe		0.92	0.9	0.92	0.93	1.06	1.05	0.31

References

1. Zhang, B.-L. *Systematic Gemology*; Geological Publishing House: Beijing, China, 2006; pp. 324–327.
2. Bruand, E.; Fowler, M.; Storey, C.; Darling, J. Apatite trace element and isotope applications to petrogenesis and provenance. *Am. Mineral.* **2017**, *102*, 75–84. [CrossRef]
3. Boyce, J.W.; Hervig, R.L. Apatite as a Monitor of Late-Stage Magmatic Processes at Volcán Irazú, Costa Rica. *Contrib. Mineral. Petrol.* **2009**, *57*, 135–145. [CrossRef]
4. Belousova, E.A.; Griffin, W.L.; O'Reilly, S.Y.; Fisher, N.I. Apatite as an indicator mineral for mineral exploration: Trace-element compositions and their relationship to host rock type. *Geochem. Explor.* **2002**, *76*, 45–69. [CrossRef]
5. Xu, B.; Hou, Z.-Q.; Griffin, W.L.; O'Reilly, S.Y. Apatite halogens and Sr–O and zircon Hf–O isotopes: Recycled volatiles in Jurassic porphyry ore systems in southern Tibet. *Chem. Geol.* **2022**, *605*, 10. [CrossRef]
6. Zhang, F.; Li, W.; White, N.; Zhang, L.; Qiao, X.; Yao, Z. Geochemical and isotopic study of metasomatic apatite: Implications for gold mineralization in Xindigou, northern China. *Ore Geol. Rev.* **2020**, *127*, 103853. [CrossRef]
7. Ren, Z.; Cui, J.; Liu, C.; Li, T.; Chen, G.; Dou, S.; Tian, T.; Luo, Y. Apatite Fission Track Evidence of Uplift Cooling in the Qiangtang Basin and Constraints on the Tibetan Plateau Uplift. *Acta Geol. Sin.-Engl. Ed.* **2015**, *89*, 467–484.
8. Li, W. Study on Gemological and Chromatic Characteristics of Blue-Green Apatite. Master's Thesis, China University of Geosciences, Beijing, China, 2021.
9. Yang, Y.-F. Gem Mineralogy of Different Colors of Apatite. Master's Thesis, China University of Geosciences, Beijing, China, 2019.
10. Rossi, M.; Ghiara, M.R.; Chita, G.; Capitelli, F. Crystal-Chemical and Structural Characterization of Fluorapatites in Ejecta from Somma−Vesuvius Volcanic Complex. *Am. Mineral.* **2011**, *96*, 1828–1837. [CrossRef]
11. Pan, Y.; Fleet, M.E. Compositions of the Apatite-Group Minerals: Substitution Mechanisms and Controlling Factors. *Rev. Mineral. Geochem.* **2002**, *48*, 13–49. [CrossRef]
12. Zhu, X.Q.; Wang, Z.G.; Huang, Y. Rare earth composition of apatite and its tracing significance. *Rare Earths* **2004**, *25*, 41–45+63. (In Chinese) [CrossRef]
13. Sha, L.-K.; Chappell, B.W. Apatite Chemical Composition, Determined by Electron Microprobe and Laser-Ablation Inductively Coupled Plasma Mass Spectrometry, as a Probe into Granite Petrogenesis. *Geochim. Cosmochim. Acta* **1999**, *63*, 3861–3881. [CrossRef]
14. Xu, B.; Hou, Z.-Q.; Griffin, W.L.; Lu, Y.; Belousova, E.; Xu, J.-F.; O'Reilly, S.Y. Recycled Volatiles Determine Fertility of Porphyry Deposits in Collisional Settings. *Am. Mineral.* **2021**, *106*, 656–661. [CrossRef]
15. Chen, N.; Pan, Y.; Weil, J.A. Electron Paramagnetic Resonance Spectroscopic Study of Synthetic Fluorapatite: Part I. Local Structural Environment and Substitution Mechanism of Gd^{3+} at the Ca2 Site. *Am. Mineral.* **2002**, *87*, 37–46. [CrossRef]
16. Fleet, M.E.; Pan, Y. Site Preference of Rare Earth Elements in Fluorapatite. *Am. Mineral.* **1995**, *80*, 329–335. [CrossRef]
17. Mao, M.; Rukhlov, A.S.; Rowins, S.M.; Spence, J.; Coogan, L.A. Apatite Trace Element Compositions: A Robust New Tool for Mineral Exploration. *Econ. Geol.* **2016**, *111*, 1187–1222. [CrossRef]
18. Rakovan, J.F.; Hughes, J.M. Strontium in the apatite structure: Strontium fluorapatite and belovite-(Ce). *Can. Mineral.* **2000**, *38*, 839–845. [CrossRef]
19. Piccoli, P.M.; Candela, P.A. Apatite in Igneous Systems. *Rev. Mineral. Geochem.* **2002**, *48*, 255–292. [CrossRef]
20. Hughes, J.M.; Ertl, A.; Bernhardt, H.-J.; Rossman, G.R.; Rakovan, J. Mn−Rich Fluorapatite from Austria: Crystal Structure, Chemical Analysis, and Spectroscopic Investigations. *Am. Mineral.* **2004**, *89*, 629–632. [CrossRef]
21. Sudarsanan, K.; Young, R.A.; Wilson, A.J.C. The Structures of Some Cadmium 'apatites' $Cd_5(MO_4)_3X$. I. Determination of the Structures of $Cd_5(VO_4)_3I$, $Cd_5(PO_4)_3Br$, $Cd_3(AsO_4)_3Br$ and $Cd_5(VO_4)_3Br$. *Acta Crystallogr. Sect. B Struct. Crystallogr. Cryst. Chem.* **1977**, *33*, 3136–3142. [CrossRef]
22. Peng, G.; Luhr, J.F.; McGee, J.J. Factors Controlling Sulfur Concentrations in Volcanic Apatite. *Am. Mineral.* **1997**, *82*, 1210–1224. [CrossRef]
23. Perseil, E.-A.; Blanc, P.; Ohnenstetter, D. As-Bearing Fluorapatite in Manganiferous Deposits from St. Marcel-praborna, val d'aosta, Italy. *Can. Mineral.* **2000**, *38*, 101–117. [CrossRef]
24. Xu, B.; Hou, Z.-Q.; Griffin, W.L.; Zheng, Y.-C.; Wang, T.; Guo, Z.; Hou, J.; Santosh, M.; O'Reilly, S.Y. Cenozoic Lithospheric Architecture and Metallogenesis in Southeastern Tibet. *Earth-Sci. Rev.* **2021**, *214*, 103472. [CrossRef]
25. Miles, A.J.; Graham, C.M.; Hawkesworth, C.J.; Gillespie, M.R.; Hinton, R.W.; Bromiley, G.D. Apatite: A New Redox Proxy for Silicic Magmas? *Geochim. Cosmochim. Acta* **2014**, *132*, 101–119. [CrossRef]
26. Che, J.Y.; Zhao, Y.D. A review of the basal characteristics of Precambrian metamorphic substrates in Madagascar. *Geol. Resour.* **2013**, *4*, 341.
27. Xu, B.; Griffin, W.L.; Xiong, Q.; Hou, Z.-Q.; O'Reilly, S.Y.; Guo, Z.; Pearson, N.; Greau, Y.; Zheng, Y.-C. Ultrapotassic rocks and xenoliths from South Tibet: Contrasting styles of interaction between lithospheric mantle and asthenosphere during continental collision. *Geology* **2017**, *45*, 51–54. [CrossRef]
28. Huang, G.P.; Hu, Q.L.; Chen, D.M.; Li, L.; Zhang, Z.; Zhu, A.A.; Xu, H.B. Overview of Geology and Mineral Resources of Madagascar. *Resour. Environ. Eng.* **2014**, *28*, 626–632.
29. Wang, H.B.; Xia, F.F.; Wu, H.X. A brief analysis of geological characteristics and minerals in Ambatondrazaka area. *Mod. Min.* **2012**, *27*, 33−34, 37.

30. Zolotarev, V.M. Optical Constants of an Apatite Single Crystal in the IR Range of 6–28 Mm. *Opt. Spectrosc.* **2018**, *124*, 262–272. [CrossRef]
31. Yuan, P.Y.; Xu, B.; Wang, Z.X.; Liu, D.Y. A Study on Apatite from Mesozoic Alkaline Intrusive Complexes, Central High Atlas, Morocco. *Crystals* **2022**, *12*, 461. [CrossRef]
32. Zhao, Z.-G.; Gao, L.-M. Standardization of δEu, δCe calculation methods. *Stand. Cover.* **1998**, *5*, 24–26.
33. Wang, R.J. Application of rare earth elements in petrology. *Geol. Sci. Technol. Inf.* **1983**, *3*, 32–39.
34. Yang, Y.-H.; Wu, F.-Y.; Yang, J.-H.; Chew, D.M.; Xie, L.-W.; Chu, Z.-Y.; Zhang, Y.-B.; Huang, C. Sr and Nd Isotopic Compositions of Apatite Reference Materials Used in U–Th–Pb Geochronology. *Chem. Geol.* **2014**, *385*, 35–55. [CrossRef]
35. Su, X.D.; Peng, P.; Wang, C.; Sun, F.B.; Zhang, Z.Y.; Zhou, X.T. Whole-rock and mineral chemical data from a profile of the ~900 Ma Niutishan Fe-Ti-rich sill in XuZhou, North China. *Data Brief* **2018**, *21*, 727–735. [CrossRef] [PubMed]
36. Takashima, R.; Kuwabara, S.; Sato, T.; Takemura, K.; Nishi, H. Utility of trace elements in apatite for discrimination and correlation of Quaternary ignimbrites and co−ignimbrite ashes, Japan. *Quat. Geochronol.* **2017**, *41*, 151–162. [CrossRef]
37. Liu, J.-W. Characterization of Granitic Apatite Speciation in Jiu Dong and Xiao Qin Ling and Its Geological Significance. Master's Thesis, China University of Geosciences, Beijing, China, 2019.
38. Liu, D.-Y. Gemological Characteristics of Apatite in Three Origins. Master's Thesis, China University of Geosciences, Beijing, China, 2021.
39. Xu, B.; Hou, Z.-Q.; Griffin, W.L.; Zhou, Y.; Zhang, Y.F.; Lu, Y.J.; Belousova., E.A.; Xu, J.F.; O'Reilly, S.Y. Elevated Magmatic Chlorine and Sulfur Concentrations in the Eocene–Oligocene Machangqing Cu–Mo Porphyry System. *SEG Spec. Publ.* **2021**, *24*, 257–276.
40. O'Reilly, S.Y.; Griffin, W.L. Apatite in the mantle: Implications for metasomatic processes and high heat production in Phanerozoic mantle. *Lithos* **2000**, *53*, 217–232. [CrossRef]
41. Chen, W.; Simonetti, A. In-situ determination of major and trace elements in calcite and apatite, and U-Pb ages of apatite from the Oka carbonatite complex: Insights into a complex crystallization history. *Chem. Geol.* **2013**, *353*, 151–172. [CrossRef]
42. Liu, X.Q.; Zhang, H.; Tang, Y.; Liu, Y.L. REE Geochemical Characteristic of Apatite: Implications for Ore Genesis of the Zhijin Phosphorite. *Minerals* **2020**, *10*, 1012. [CrossRef]
43. Prowatke, S.; Klemme, S. Trace element partitioning between apatite and silicate melts. *Geochim. Cosmochim. Acta* **2006**, *70*, 4513–4527. [CrossRef]
44. Xu, B.; Hou, Z.-Q.; Griffin, W.L.; O'Reilly, S.Y.; Zheng, Y.-C.; Wang, T.; Fu, B.; Xu, J.F. In-situ mineralogical interpretation of the mantle geophysical signature of the Gangdese Cu-porphyry mineral system. *Gondwana Res.* **2022**, *111*, 53–63. [CrossRef]